

## Supplementary Information

### **Realization of ppm-level CO detection with an exceptionally high sensitivity using reduced graphene oxide-loaded SnO<sub>2</sub> nanofibers with the Au functionalization**

Jae-Hun Kim,<sup>a</sup> Akash Katoch,<sup>a</sup> Hyoun Woo Kim,<sup>\*b</sup> Sang Sub Kim,<sup>\*a</sup>

<sup>a</sup> *Department of Materials Science and Engineering, Inha University, 100 Inha-ro, Nam-gu, Incheon 402-751, Republic of Korea E-mail: sangsub@inha.ac.kr; Fax: +82-32-862-5546; Tel: +82-32-860-7546*

<sup>b</sup> *Division of Materials Science and Engineering, Hanyang University, 222 Wangsimni-ro, Seongdong-Gu, Seoul, 133-791, Republic of Korea. E-mail: hyounwoo@hanyang.ac.kr; Tel: +82-2220-0382*

## Text S1.

1. For example, NO<sub>2</sub> responses of SnO<sub>2</sub>-coated carbon nanotubes or reduced graphene oxide (RGO) sensors were remarkably enhanced due to the formation of a heterojunction between a carbon support and an SnO<sub>2</sub> [S1]. Graphene/Cu<sub>2</sub>O heterostructures, in which graphene sheets were functionalized with Cu<sub>2</sub>O crystals, have achieved the room temperature detection of H<sub>2</sub>S [S2]. WO<sub>3</sub> hemitubes modified by graphite or GO layers were proposed for the diagnosis of diabetes and halitosis [S3]. More recently, we have synthesized RGO nanosheet (NS)-loaded SnO<sub>2</sub> nanofibers (NFs) that showed significantly improved gas sensing capability when loaded with an optimized amount of RGO NSs, in comparison to bare SnO<sub>2</sub> NFs [S4].
2. First, Au doping has been carried out to form Au-doped SnO<sub>2</sub> powder [S5] and Au-doped thin films [S6]. Second, a Au shell was formed on SnO<sub>2</sub> to fabricate Au nanoparticle-decorated porous SnO<sub>2</sub> hollow spheres [S7], Au-decorated SnO<sub>2</sub> nanobelts [S8], Au@SnO<sub>2</sub> yolk-shell nanospheres [S9], Au@SnO<sub>2</sub> core/shell nanoparticles [S10], and SnO<sub>2</sub> thin films covered with Au layers [S11]. Third, a SnO<sub>2</sub> shell was covered on Au, yielding SnO<sub>2</sub>@Au core/shell nanoparticles [S12].

## **Text S2. Experimental Methods**

### **Materials**

Zinc acetate ( $(\text{CH}_3\text{CO}_2)_2\text{Zn}$ ), reduced graphene oxide (rGO), polyvinyl alcohol (MW 80,000), tin(II) chloride dihydrate, polyvinylpyrrolidone (MW 13,00,000), ethanol (anhydrous, 99.5%), and dimethylformamide (DMF, anhydrous, 99.8%) were obtained from Sigma Aldrich Corp. and were used as received without any further processing or refining.

### **Preparation of RGO NSs**

Graphene oxide (GO) was synthesized from graphite powder by a modified Hummers and Offeman method [S13]. To reduce the prepared GO, 10 ml of hydrazine monohydrate was added into the GO suspension, and the mixture was heated at 150 °C for 24 hours. The products were then isolated by centrifugation at 12,000 rpm for 45 min and washed with DI water and methanol until pH=7 to yield pure RGO powder.

### **Preparation of Au-functionalized RGO NSs-loaded SnO<sub>2</sub>**

Tin (II) chloride dihydrate ( $\text{SnCl}_2 \cdot 2\text{H}_2\text{O}$ , Sigma-Aldrich Corp.), polyvinyl acetate

(PVAc,  $M_w = 850,000$ , Sigma-Aldrich Corp.), ethanol (anhydrous, 99.5%, Sigma-Aldrich Corp.), dimethylformamide (DMF, anhydrous, 99.8%, Sigma-Aldrich Corp.), hydrogen tetrachloroaurate (III) hydrate ( $\text{HAuCl}_4 \cdot n\text{H}_2\text{O}$ ,  $n=3.5$ , Kojima Chemical Co.) and de-ionized (DI) water were used as the starting materials without any further purification.

For synthesis of Au-functionalized RGO NSs-loaded  $\text{SnO}_2$  NFs (hereafter, Au-functionalized RGO NSs- $\text{SnO}_2$  NFs), sol-gel and electrospinning methods were used and are schematically described in Fig. 1. First, an aqueous PVAc solution was prepared by dissolving PVAc beads in the mixed solvent of ethanol (20 g) and DMF (15g) with constant stirring for 6 hours. Then,  $\text{SnCl}_2 \cdot \text{H}_2\text{O}$  (2.7 g) was added to prepared the PVAc solution and was stirred for 10 h. Subsequently, an aqueous solution of  $\text{HAuCl}_2 \cdot n\text{H}_2\text{O}$  was prepared separately by mixing 0.0007 g of  $\text{HAuCl}_4 \cdot n\text{H}_2\text{O}$  with isopropanol followed by constant stirring for 1 hour. The prepared Au precursor solution was then exposed to UV radiation ( $\lambda = 360 \text{ nm}$ , intensity =  $0.1 \text{ Mw/cm}^2$ ) for 1 min. This led to the growth of Au nanoparticles (NPs) in solution. Then, the prepared Au NP suspension and 0.44 wt% RGO NSs were mixed into the PVAc/ $\text{SnCl}_2 \cdot \text{H}_2\text{O}$  solution (For the fabrication of Au-functionalized  $\text{SnO}_2$  NFs and RGO NSs- $\text{SnO}_2$  NFs, Au NP suspension and 0.44 wt% RGO NSs were mixed into the PVAc/ $\text{SnCl}_2 \cdot \text{H}_2\text{O}$  solution, respectively). Vigorous stirring for 1 hour eventually resulted in the formation of a viscous solution of PVAc/ $\text{SnCl}_2 \cdot \text{H}_2\text{O}$  containing Au NPs and RGO NSs. The prepared precursor solution was loaded into a syringe with a 21-gauge needle with an inner diameter of 0.51 mm. The composite fibers were electrospun by applying 15 kV using a

DC power supply with a distance of 20 cm between the tip of the needle and a ground plate. The feeding rate of the solution was adjusted accurately to a constant value of 0.03 ml/h. The electrospun fibers were obtained over the SiO<sub>2</sub>-grown Si wafers that had been placed on the metal collector. All the electrospinning experiments were carried out at room temperature. The as-spun fibers were subsequently calcined at a temperature of 600 °C for 30 min in air with a heating rate of 2 °C/min. The synthesis procedure for nanofibers by electrospinning is described in detail in our previous report [S14].

In this work, we have loaded 0.44 wt% RGO into SnO<sub>2</sub> NFs because that amount of loading exhibited the best gas-sensing performance for SnO<sub>2</sub> NFs in comparison to the case of less or more RGO loading [S4]. It is known that the RGO is stable at temperatures in the range of -10 to 800°C [S15,S16]. Furthermore, the TGA analysis, by means of using the STA 409 PC (NETZSCH), for the RGO NS-loaded SnO<sub>2</sub> NFs indicated that RGO was stable up to 900°C [S4]. In addition, we have functionalized Au with 1 at% by changing the amount of the Au-containing solution in the electrospinning solution. In our earlier report [S17], the sensing capabilities of the sensors fabricated with the Au-loaded SnO<sub>2</sub> NFs were systematically investigated as a function of the amount of Au loading. The CO response of the sensors was significantly improved by loading Au into SnO<sub>2</sub> NFs. The highest response was observed for the sensor with ~1.7 at% Au-loaded SnO<sub>2</sub> NFs, along with the very high selectivity to CO gas, compared with other gases, including toluene, ethanol, H<sub>2</sub>S, CO<sub>2</sub>, and benzene. Further loading of Au decreased the sensor response, suggesting that an optimization of the amount of Au loading is crucial to maximize the sensing properties of SnO<sub>2</sub> NFs. On the basis of this

investigation, we realized that the 1 at% of Au loading should be enough to obtain the high sensing capabilities.

### **Materials characterization and sensing measurement**

The morphology of the Au-functionalized RGO NSs-SnO<sub>2</sub> NFs was investigated using scanning electron microscopy (SEM, Hitachi S-4200). The phase of samples was examined by X-ray diffraction (XRD, Philips X'pert MRD diffractometer) using Cu K $\alpha$  radiation ( $\lambda = 1.5406 \text{ \AA}$ ). In addition, the samples were investigated by transmission electron microscopy (TEM, Philips CM-200), being accompanied by an energy-dispersive X-ray spectrometer (EDX).

For the sensing measurements, Pt (~200 nm) and Ti (~50 nm) were sequentially deposited via sputtering on the specimens using an interdigital electrode mask, being similar to the previous reports [S18-S21]. The sensing abilities of the Au-functionalized RGO NSs-SnO<sub>2</sub> NFs were measured in terms of reducing gases (CO, C<sub>6</sub>H<sub>6</sub> and C<sub>7</sub>H<sub>8</sub>) using a gas dilution and sensing system. In order to determine optimal operating temperature of the sensors, various operating temperatures in the range of 100-450 °C were investigated. The gas concentration was controlled by changing the mixing ratio of target gas to dry air through accurate mass flow controllers (MFCs). The total flow rate was set to 500 sccm to avoid any possible variation in sensing performance. The gas response was evaluated using the formula  $R = R_a/R_g$ , where  $R_a$  and  $R_g$  are the resistance in the absence and presence of reducing target gas, respectively.

### **Text S3.**

In the case of pristine SnO<sub>2</sub> NF sensors, prior to the introduction of CO gas, there exists an electron depletion region not only on the SnO<sub>2</sub> NF surface, but also at the SnO<sub>2</sub> nanograin boundaries, due to the adsorption of oxygen species in air ambient (Fig. 5(a) in the main text). Oxygen species, which have diffused onto the grain boundaries, take out electrons from the grain boundaries. Upon the introduction of CO gas, the CO molecule always acts as an electron donor [S22]. It decreases the concentration of ionized oxygen species by generating volatile molecules, resulting in an increase in charge carrier concentration, and thus a reduction of resistance. Accordingly, electron transfer from adsorbed CO to SnO<sub>2</sub> will increase the electron concentration, thereby decreasing the resistivity in SnO<sub>2</sub>. By means of the introduction of CO gas, the electron depletion region will shrink. In addition, the grain boundaries in the SnO<sub>2</sub> NFs provide the potential barrier, with the upward bending in air ambient (Fig. 5a in the main text). Upon the introduction of target gas, CO molecules adsorb and react with chemisorbed oxygen in the grain boundaries, reducing the potential barriers and thus increasing the conductivity, generating the additional modulation of resistance. Both the radial modulation of the electron depletion region and the potential barrier modulation at grain boundaries are the primary source of resistance change during adsorption and desorption of gas molecules. This is schematically described in Fig. 5(a) in the main

text. Although the modulation of resistance will occur via contact of neighboring NFs, this part of resistance will be negligible in comparison to others [S4].

#### **Text S4.**

In order to investigate the selective gas sensing properties of the Au-functionalized RGO NSs-SnO<sub>2</sub> NFs sensors with regard to CO gas, their responses to other gases such as C<sub>6</sub>H<sub>6</sub> and C<sub>7</sub>H<sub>8</sub> were measured at 400°C (Fig. 4(a) in the main text). When the sensors are exposed to reducing gases including CO, C<sub>6</sub>H<sub>6</sub> and C<sub>7</sub>H<sub>8</sub>, the resistance rapidly decreases. When the supply of the reducing gases is stopped with the introduction of air, the resistance almost completely returns to the initial values. In comparison to the previous results of RGO NS-loaded SnO<sub>2</sub> NFs [S4], the addition of Au NPs increased the resistance of the resultant sensing material from around 400 K ohm to 40 M ohm. A lot of Au NPs are distributed in the matrix of SnO<sub>2</sub> NFs, forming local heterojunctions at which electrons in SnO<sub>2</sub> flow toward Au. The addition of Au NPs to SnO<sub>2</sub> NFs increases the resistance of the NFs, due to the electron transfer from the conduction band of SnO<sub>2</sub> to Au (i.e. the work function of Au is around 5.1 eV and that of SnO<sub>2</sub> is 4.55 eV). Fig. 4(b) (in the main text) shows a summary of sensor responses to the measured gases, including CO, C<sub>6</sub>H<sub>6</sub> and C<sub>7</sub>H<sub>8</sub>, for the Au-functionalized RGO NSs-SnO<sub>2</sub> NFs sensors, revealing that the sensor has a highly selective sensing capability toward CO gas.

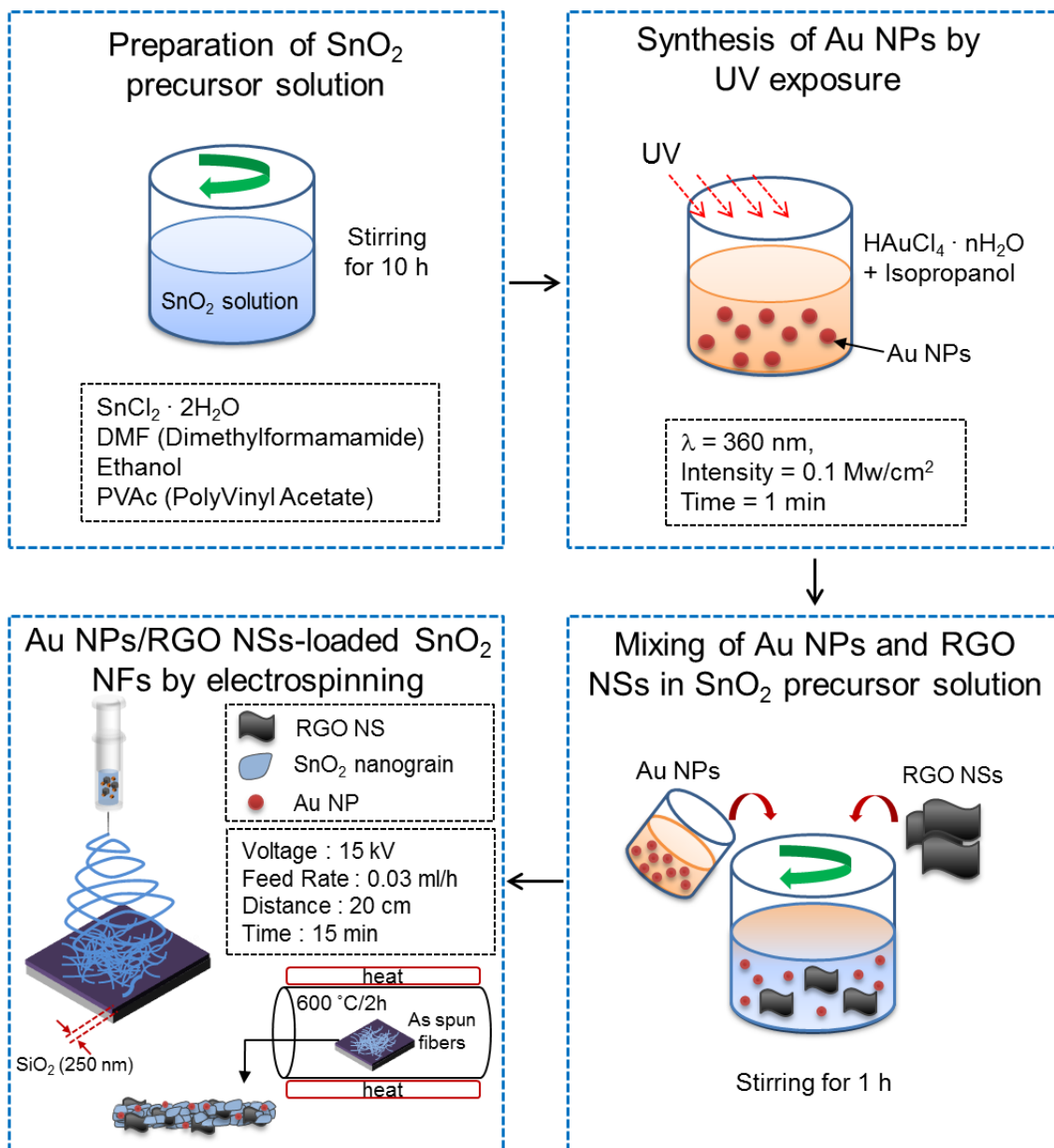


**Fig. S1.** Schematic illustration of the fabrication for Au-functionalized RGO nanosheets-SnO<sub>2</sub> nanofibers.

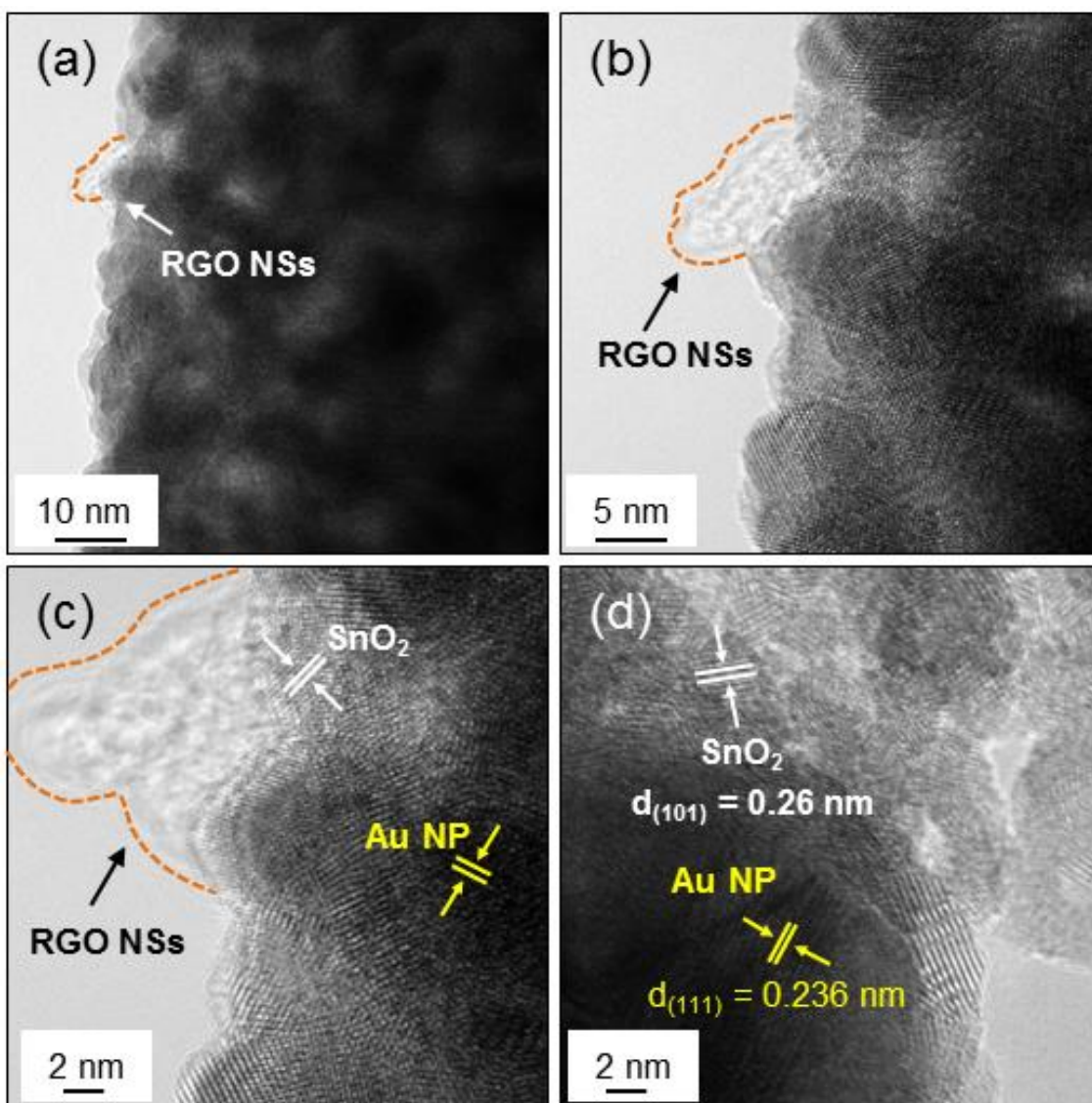


**Fig. S2.** (a) TEM image of a NF. (b) Enlarged TEM image. (c,d) Lattice-resolved TEM images enlarging a surface region, indicating the presence of Au NPs and RGO NSs.

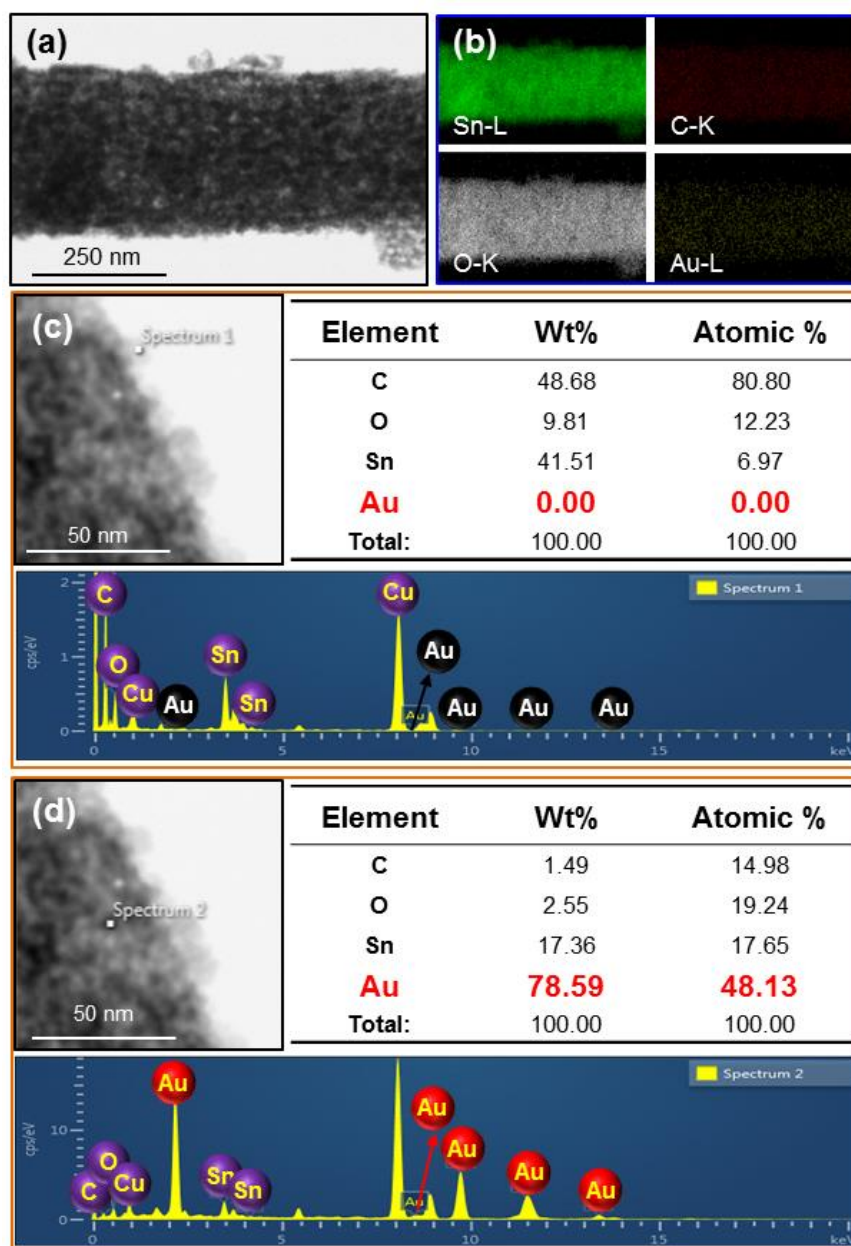


**Fig. S3.** (a) TEM image of a NF and (b) corresponding elemental maps of Sn, C, O, and Au elements. (c,d) EDX spectra from the region (c) without and (d) with Au NPs. They are comprised of TEM images, EDX spectra, and tables representing the compositions of C, O, Sn, and Au elements.

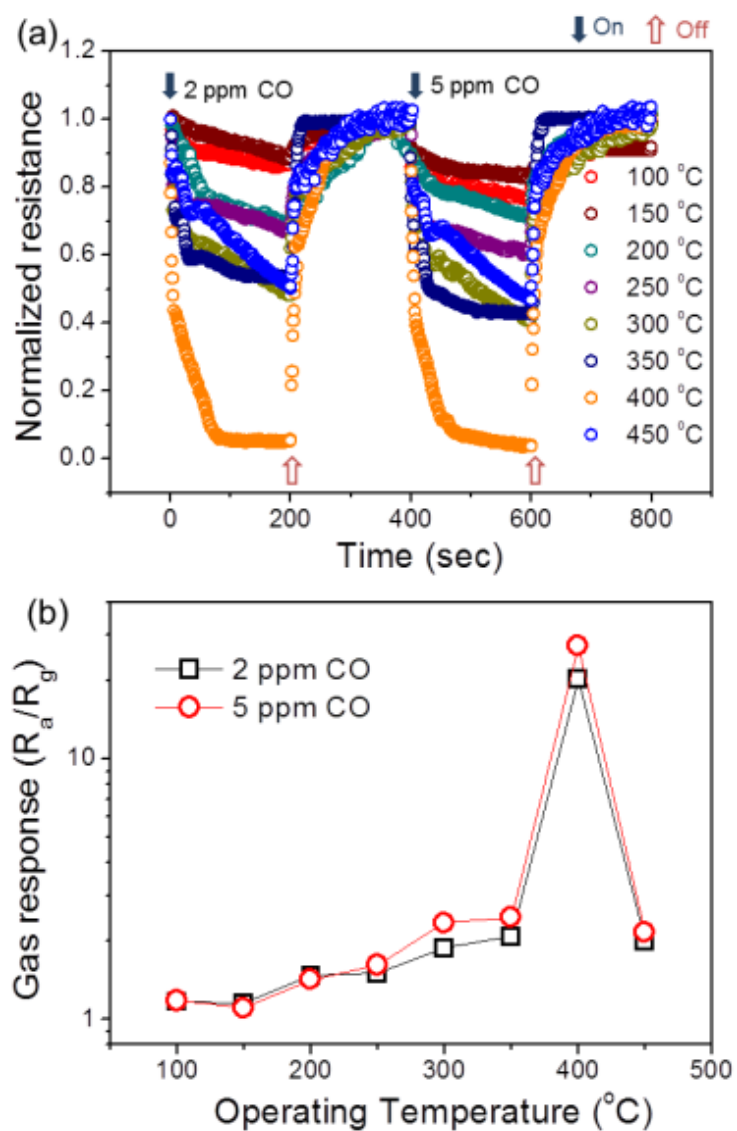


**Fig. S4.** (a) Dynamic response curves of Au-functionalized RGO nanosheets-SnO<sub>2</sub> nanofibers. Each curve was plotted for CO concentration of 2 and 5 ppm, respectively, at temperatures in the range of 100-450°C. (b) Change of sensor response of the Au-functionalized RGO nanosheets-SnO<sub>2</sub> nanofibers as a function of operating temperatures.

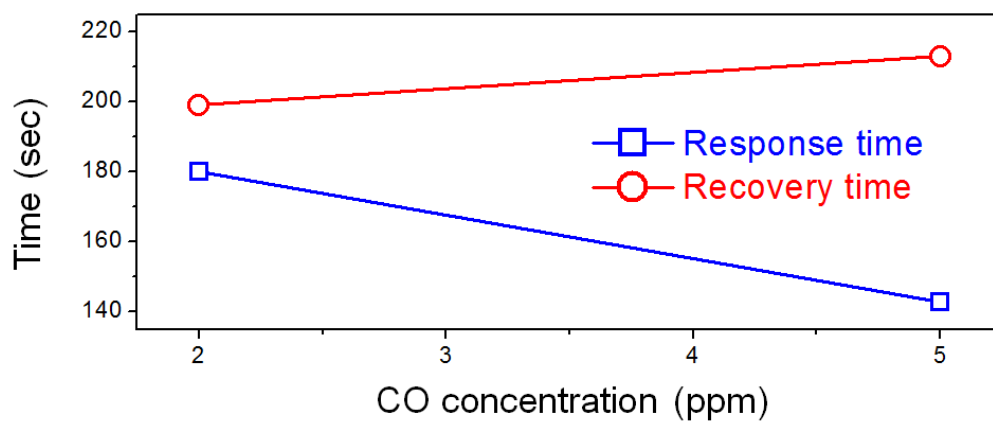


**Fig. S5.** Response time and recovery time of the Au-functionalized RGO NSs-SnO<sub>2</sub> NFs at 2 and 5 ppm.

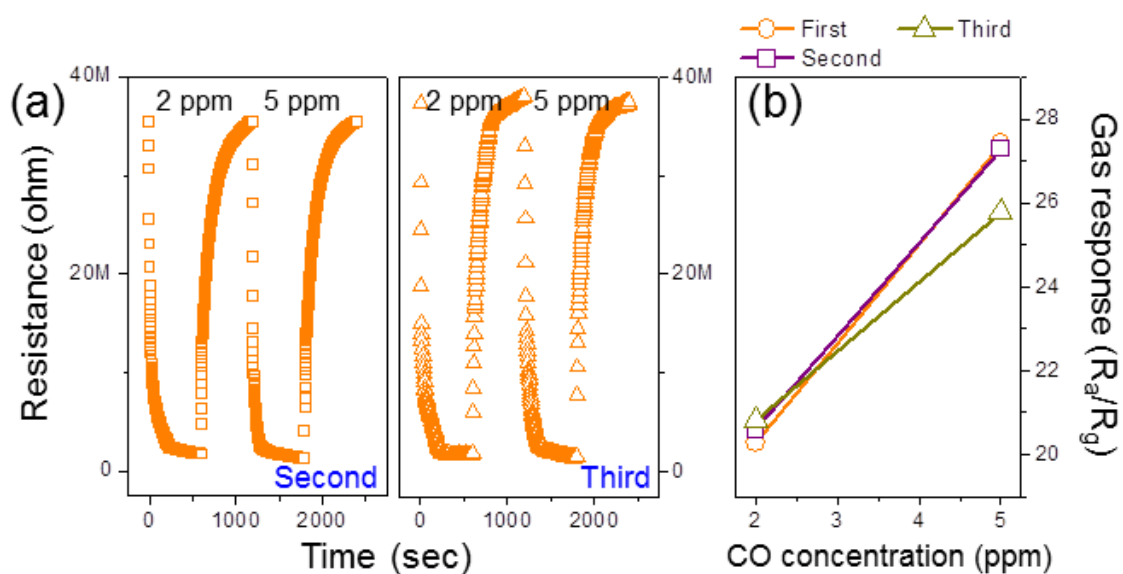


**Fig. S6.** Dynamic resistance curves of the Au-functionalized RGO NSs-SnO<sub>2</sub> NFs at 2 and 5 ppm, for second and third cycles. (b) Sensor responses of the Au-functionalized RGO NSs-SnO<sub>2</sub> NFs at 2 and 5 ppm, for first, second, and third cycles.

**Table S1** CO sensor responses of the recently developed semiconductor sensors consisting of a variety of materials.

Nanostructure type	Gas concentration (ppm)	Temperature (°C)	Response ( $R_a/R_g$ or $R_o/R_a$ )	Temp./Conc. At optimal sensing	Reference
Au-doped SnO <sub>2</sub> -In <sub>2</sub> O <sub>3</sub> nanocomposites (2007)	500-1,000	25-350	480	50/1000	S23
SnO <sub>2</sub> -In <sub>2</sub> O <sub>3</sub> nanocomposites (2007)	500-1,000	25-350	16	50/1000	S23
Au and SnO <sub>2</sub> nanocrystals on CNTs (2008)	500-2500	25	30	25/500	S24
Au-decorated ZnO nanowires (2009)	100-1000	25-200	0.9	200/100	S25
In <sub>2</sub> O <sub>3</sub> hierarchical microspheres (2009)	400	10-50	2.16 (3.81)	400/10(50)	S26
Graphene films (2010)	100	25-200	1.03	25/100	S27
ZnO/Au thin films (2010)	5-70	150-400	6.4	250/20	S28
Au nanoparticles-functionalized In <sub>2</sub> O <sub>3</sub> nanowires FET (2011)	0.2-5	25	104 ~36	25/5 25/1	S29
Hexagonal-shaped CdO nanostructures (2012)	25-75	150-350	~1.24	250/75	S20
Hierarchically porous ZnO nanosheet thin films (2012)	5-500	200-380	11.2 (1.7)	300/100(5)	S31
Hollow CuTe nanocrystals (2012)	5-500	180-360	1.11 (1.37)	260/5 (100)	S32
Pd nanodot-functionalized ZnO nanowires (2012)	0.1-2	25	1.02	25/0.1	S33
Au@TiO <sub>2</sub> core-shell nanoparticles (2013)	200-1000	500-600	1.21	600/1000	S34
PdO nanoflake thin films (2013)	250-4000	50-250	1.1	100/250	S35
Porous titania with heavily self-doped Ti <sup>3+</sup> (2013)	100-10,000	25	1.7	25/100	S36
Pt-loaded SnO <sub>2</sub> porous nanosolid (2013)	50-1000	25	64.5	25/100	S37
Co <sub>3</sub> O <sub>4</sub> nanowires (2014)	10-200	100	3 29	100/10 100/200	S38
Nanocrystalline LaCaFeO <sub>3</sub> (2014)	200-2000	120-370	~6 (3.5)	180/2000(200)	S39
Pd and Fe-doped SnO <sub>2</sub> (2014)	200-3000	200-400	~30	200/2000	S40
Pt/SnO <sub>2</sub> (2014)	100	250	160	100/250	S41
Sm <sub>2</sub> O <sub>3</sub> -doped Pt/SnO <sub>2</sub> (2014)	100	250	215.9	100/250	S41
In <sub>2</sub> O <sub>3</sub> raspberry hollow spheres (2015)	1-100	200	96 7	200/100 200/1	S42
Nanostructured Co <sub>3</sub> O <sub>4</sub> (2015)	1-25	200-290	1.2 (2.1)	200/1(25)	S43
<b>Au-functionalized RGO-loaded SnO<sub>2</sub> nanofibers</b>	<b>2-5</b>	<b>100-450</b>	<b>20.3 (27.4)</b>	<b>400/2 (5)</b>	<b>Present work</b>

## References

- 1 C. Marichy, P. A. Russo, M. Latino, J.-P. Tessonier, M.-G. Willinger, N. Donato, G. Neri and N. Pinna, *J. Phys. Chem. C*, 2013, 117, 19729-19739.
- 2 L. Zhou, F. Shen, X. Tian, D. Wang, T. Zhang and W. Chen, *Nanoscale*, 2013, 5, 1564-1569.
- 3 S.-J. Choi, F. Fuchs, R. Demadrille, B. Grévin, B.-H. Jang, S.-J. Lee, J.-H. Lee, H. L. Tuller and I.-D. Kim, *ACS Appl. Mater. Interfaces*, 2014, 6, 9061-9070.
- 4 J.-H. Lee, A. Katoch, S.-W. Choi, J.-H. Kim, H. W. Kim and S. S. Kim, *ACS Appl. Mater. Interfaces*, 2015, 7, 3101-3109.
- 5 B. Bahrami, A. Khodadadi, M. Kazemeini and Y. Mortazavi, *Sens. Actuators, B*, 2008, 133, 352-356.
- 6 N. S. Ramgir, Y. K. Hwang, S. H. Jhung, H.-K. Kim, J.-S. Hwang, I. S. Mulla and J.-S. Chang, *Appl. Surf. Sci.*, 2006, 252, 4298-4305.
- 7 J. Zhang, X. Liu, S. Wu, M. Xu, X. Guo and S. Wang, *J. Mater. Chem.*, 2010, 20, 6453-6459.
- 8 L. H. Qian, K. Wang, Y. Li, H. T. Fang, Q. H. Lu and X. L. Ma, *Mater. Chem. Phys.*, 2006, 100, 82-84.
- 9 L. Wang, H. Dou, Z. Lou and T. Zhang, *Nanoscale*, 2013, 5, 2686-2691.

- 10 K. Yu, Z. Wu, Q. Zhao, B. Li and Y. Xie, *J. Phys. Chem. C*, 2008, 112, 2244-2247.
- 11 P. Nelli, G. Faglia, G. Sberveglieri, E. Cereda, G. Gabetta, A. Dieguez, A. Romano-Rodriguez and J. R. Morante, *Thin Solid Films*, 2000, 371, 249-253.
- 12 G. Oldfield, T. Ung and P. Mulvaney, *Adv. Mater.*, 2000, 12, 1519-1522.
- 13 W. S. Hummer and R. E. Offeman, *J. Am. Chem. Soc.*, 1958, 80, 1339.
- 14 J. Y. Park, K. Asokan, S.-W. Choi and S. S. Kim, *Sens. Actuators, B*, 2011, 152, 254-260.
- 15 S. Stankovich, D. A. Dikin, R. D. Piner, K. A. Kohlhaas, A. Kleinhammes, Y. Jia, Y. Wu, S. T. Nguten and R. S. Ruoff, *Carbon*, 2007, 45, 1558-1565.
- 16 P. Cui, J. Lee, E. Hwang and H. Lee, *Chem. Commun.*, 2011, 47, 12370-12372.
- 17 A. Katoch, J.-H. Byun, S.-W. Choi and S. S. Kim, *Sens. Actuators, B*, 2014, 202, 38-45.
- 18 S.-W. Choi, J. Y. Park and S. S. Kim, *Nanotechnology*, 2009, 20, 465603-465608.
- 19 J. Y. Park, S.-W. Choi, J. W. Lee, C. Lee and S. S. Kim, *J. Am. Ceram. Soc.*, 2009, 92, 2551-2554.
- 20 H. W. Kim, S. H. Shim, J. W. Lee, J. Y. Park and S. S. Kim, *Chem. Phys. Lett.*, 2008, 456, 193-197.

- 21 J. Y. Park, S.-W. Choi and S. S. Kim, *Nanoscale Res. Lett.*, 2010, 5, 353-359.
- 22 O. Leenaerts, B. Partoens and F. M. Peeters, *Phys. Rev. B*, 2008, 77, 125416.
- 23 J. T. McCue and J. Y. Ying, *Chem. Mater.*, 2007, 19, 1009-1015.
- 24 N. Du, H. Zhang, X. Ma and D. Yang, *Chem. Commun.*, 2008, 2008, 6182-6184.
- 25 R. K. Joshi, Q. Hu, F. Alvi, N. Joshi and A. Kumar, *J. Phys. Chem. C*, 2009, 113, 16199-16202.
- 26 K.-I. Choi, H.-R. Kim and J.-H. Lee, *Sens. Actuators, B*, 2009, 138, 497-503.
- 27 R. K. Joshi, H. Gomez, F. Alvi and A. Kumar, *Phys. Chem. C*, 2010, 114, 6610-6613.
- 28 N. L. Hung, H. Kim, S.-K. Hong and D. Kim, *Sens. Actuators, B*, 2010, 172, 127-132.
- 29 N. Singh, R. K. Gupta and P. S. Lee, *ACS Appl. Mater. Interfaces*, 2011, 3, 2246-2252.
- 30 S. Raj, T. Krishnakumar, R. Jayaprakash, T. Prakash, G. Leonardi and G. Neri, *Sens. Actuators, B*, 2012, 172, 853-859.
- 31 Y. Zeng, L. Qiao, Y. Bing, M. Wen, B. Zou, W. Zheng, T. Zhang and G. Zou, *Sens. Actuators, B*, 2012, 173, 897-902.
- 32 G. Xiao, Y. Zeng, Y. Jiang, W. Zheng, B. Liu, X. Chen, G. Zou and B. Zou, *Small*, 2013, 9, 793-799.
- 33 S.-W. Choi and S. S. Kim, *Sens. Actuators, B*, 2012, 168, 8-13.

- 34** Y.-S. Kim, P. Rai and Y.-T. Yu, *Sens. Actuators, B*, 2013, 186, 633-639.
- 35** Y.-J. Chiang and F.-M. Pan, *J. Phys. Chem. C*, 2013, 117, 15593-15601.
- 36** J. Su, X.-X. Zou, Y.-C. Zou, G.-D. Li, P.-P. Wang and J.-S. Chen, *Inorg. Chem.*, 2013, 52, 5924-5930.
- 37** K. Wang, T. Zhao, G. Lian, Q. Yu, C. Luan, Q. Wang and D. Cui, *Sens. Actuators, B*, 2013, 184, 33-39.
- 38** Z. Dou, C. Cao, Y. Chen and W. Song, *Chem. Commun.*, 2014, 2014, 14889-14891.
- 39** C. Shi, H. Qin, M. Zhao, X. Wang, L. Li and J. Hu, *Sens. Actuators, B*, 2014, 190, 25-31.
- 40** X.-T. Yin and X.-M. Guo, *Sens. Actuators, B*, 2014, 200, 213-218.
- 41** S. Vahdatifar, A. A. Khodadadi and Y. Mortazavi, *Sens. Actuators, B*, 2014, 191, 421-430.
- 42** A. Shanmugasundaram, P. Basak, S. V. Manorama, B. Krishna and S. Sanyadanam, *ACS Appl. Mater. Interfaces*, 2015, 7, 7679-7689.
- 43** S. Vetter, S. Haffer, T. Wagner and M. Tiemann, *Sens. Actuators, B*, 2015, 206, 133-138.